
# An adaptive power split strategy with a load disturbance compensator for fuel cell/supercapacitor powertrains

Journal of Energy Storage 44 (2021) 103341

Contents lists available at ScienceDirect

Journal of Energy Storage

journal homepage: www.elsevier.com/locate/est

Research Papers

# An adaptive power split strategy with a load disturbance compensator for fuel cell/supercapacitor powertrains☆

Qian Xun [a,*], Vicente Roda [b], Yujing Liu [a], Xiaoliang Huang [a], Ramon Costa-Castelló [b]

[a] Department of Electrical Engineering at the Chalmers University of Technology, Gothenburg 41296, Sweden
[b] Institut de Robòtica i Informàtica Industrial, CSIC-UPC, Barcelona, Spain

ARTICLE INFO

*Keywords:*
Fuel cell
Supercapacitor
Power allocation
Cut-off frequency
Load disturbance compensator

ABSTRACT

Electric vehicles powered by fuel cell and supercapacitor hybrid power sources are of great interest. However, the power allocation between each power source is challenging and the DC bus voltage fluctuation is relatively significant in cascaded PI control schemes. This paper develops a power control strategy with an adjustable cut-off frequency, using an artificial potential field, to adaptively split the load current between the fuel cell and the supercapacitor under various load conditions. The adaptive cut-off frequency is calculated by cutting the load frequency spectrum with an allocation ratio that changes with the supercapacitor state of charge. Therefore, the relatively lower frequency portion of the load current is provided by the fuel cell and the supercapacitor handles the higher frequency portion. To enhance the control performance of the DC bus voltage regulation against the load disturbance, a load disturbance compensator is introduced to suppress the DC bus voltage fluctuation when the load variation occurs, which is implemented by a feed-forward controller that can compensate the load current variation in advance. The effectiveness of the proposed strategy is validated by extensive experiments.

## 1. Introduction

The urgent environmental issues and significant advances in today's transportation sector are calling for green and sustainable solutions that can reduce $CO_2$ emissions and keep acceptable driving performance compared with internal combustion engine vehicles. Fuel cell electric vehicles (FCEVs) are becoming a promising solution for future fossil-free transportation due to their fast-refueling time, high energy density, and zero $CO_2$ emissions [1]. However, the slow-dynamic response and inability to recover regenerative energy of the FC necessitate the use of a battery or supercapacitor (SC) to form a hybrid powertrain. Compared to batteries, SCs feature high-power density and high-dynamic response, which can support the FC to meet the power requirement of vehicles, especially in such conditions with very high peak power demand and large power variation rate [2–5]. This combination can also downsize the FC power rating and extend the FC lifetime as the SC can provide more peak power during transients such as frequent start and stop, quick acceleration and deceleration, and sudden load changes [6–8].

Due to unique characteristics of FC and SC themselves, there are several hybridization structures, including passive, semi-active and fully active [9,10]. The passive hybrid system, without any DC/DC converters, shows the superiority in the conceptual structure but the DC-link voltage and the power distribution are passively determined, which is coupled with the internal resistance of each device. Due to one or two DC/DC converters involved, semi-active and fully-active hybrid systems can achieve more flexible control capability. The parameter design of FC and SC is not restricted by the DC-link voltage level and the current control is independently implemented by their converters, especially in a fully-active hybrid configuration. This hybrid configuration is also a widely employed topology in electric powertrains. To effectively utilize the power and energy capability of each power device, the control system of a fully-active hybrid powertrain is decomposed in different levels, including converter level (current tracking in most cases), power balance level (voltage bus regulation) and energy state control [11,12].

☆ This paper develops Xun, Liu, and Huang (2020) presented at IEEE Transportation Electrification Conference & Expo (ITEC), Chicago, IL, USA, 23–26 June 2020. This work was supported by the Swedish Electromobility Center and the Swedish Energy Agency, in part by the Spanish national project DOVELAR ref. RTI2018-096001-B-C32 (MCIU/AEI/FEDER, UE), and in part by the Spanish State Research Agency through the María de Maeztu Seal of Excellence to IRI (MDM-2016-0656).

* Corresponding author.
*E-mail addresses:* qian.xun@chalmers.se (Q. Xun), vicente.roda@upc.edu (V. Roda), yujing.liu@chalmers.se (Y. Liu), xiaoliang.huang@chalmers.se (X. Huang), ramon.costa@upc.edu (R. Costa-Castelló).

https://doi.org/10.1016/j.est.2021.103341
Received 30 June 2021; Received in revised form 2 September 2021; Accepted 27 September 2021
Available online 16 November 2021

Existing power management strategies are usually based on rules, artificial intelligence, or optimization. To meet the vehicle power requirement and enhance the FC performance, a fuzzy logic-based control method is implemented in [13,14]. To achieve the same goals, the vehicle power demand is decomposed into low- and high-frequency item using a wavelet-based algorithm in [15]. The simulation results show the effectiveness of the proposed method and the sharp peak load is provided by the SC with the FC power variation to be smoothed. However, the algorithm is not experimentally verified and it is complicated to implement in real-time control applications. In [16], a control law based on differential flatness is proposed to achieve energy-management goals and solve the stabilization issue. The proposed control law is validated in dSPACE based implementation on an experimental test rig. The results show that power provided by the FC and the SC can meet the load demand and the DC-link voltage variation is significantly improved compared with the classical PI controller. However, the experimental verification is limited to investigate the step load variation and the half-sine waveform while the drive cycle performance is not evaluated. A frequency-based power distribution method is presented in [17] to find an optimal set point of the cut-off frequency based on the dynamic capabilities of each energy source while it only shows the simulation results. Some other control strategies, such as state machine control [18], droop control [19], and extremum seeking [20], are conducted on RT-LAB platform for fuel cell hybrid electric trams. The control strategies can manage and coordinate multiple power sources and meet the tram power requirement.

In addition, dynamic programming based energy management strategy is studied in [21] to obtain the optimal power split between each device. An energy management control strategy with the prediction of a short-period future energy demand is detailed reported in [22]. The energy flow control is emphasized for FC/SC electric vehicles to minimize the hydrogen consumption and improve the power compliance. Optimal energy management and control frameworks are presented in [23–25] to improve the global performance of the system. A cost function is usually formulated as a mathematical extreme value problem with several constraints to minimize equivalent energy consumption and improve the utilization performance of the system. For example, model predictive control is utilized to improve the system performance, such as fuel economy and fuel cell lifetime [26,27] by solving a multi-objective optimization problem. In [28], a comparative study on five commonly-used energy management strategies for fuel cell hybrid power sources are investigated. The results show that the state machine control provides slightly better efficiency and less stresses on battery and SC than other strategies. By contrast, the conventional PI control shows better fuel economy and more usable battery energy. In [29,30], several energy management strategies are reviewed, their control objectives, strengths, weaknesses and applications are discussed. The principles, recent progress and outlook of multiple energy management strategies are reported in [31].

Among all power allocation methods, filter-based methods (i.e., a subset of rule-based methods) are widely adopted in real-time applications. A low-pass filter or a high-pass filter is employed to split the load power into low-frequency and high-frequency parts. The low-frequency part is fed to the FC and the high-frequency part is provided by the SC. However, the cut-off frequency is highly dependent on the vehicle specifications and the driving conditions. Therefore, it is challenging to determine a constant frequency suitable for all driving conditions. Moreover, the load current is treated as the disturbance in the conventional PI controller design, which results in DC bus voltage fluctuations when the load changes for example when the vehicle frequently accelerates or decelerates.

To make the filter-based method applicable for all driving conditions, an adaptive cut-off frequency has been proposed by several researchers. [32] implemented one off-line optimized cut-off frequency in battery/supercapacitor hybrid energy storage system according to the vehicle speed, road condition and load current, and the experimental results show good performance. Also, [33] proposes an optimal cut-off frequency according to the off-line data using dynamic programming. In [34], a varying frequency splitter is also applied in the same hybrid energy storage system, the cut-off frequency is calculated according to the output of the DC-link voltage controller and the SC state of charge (SoC), and the time constant of the low-pass filter is empirically set by a look-up table with three fixed time-constants. The experimental results show the feasibility of the proposed power-split method. In [35], a more flexible cut-off frequency is selected by cutting the length of the load current spectrum with a constant allocation ratio. Nevertheless, the SC cannot avoid over-discharge or over-charge based on the constant allocation ratio. To solve this issue, [36] proposes an adaptive frequency method with the allocation ratio changing with the SC SoC based on artificial potential field and the SC SoC can be effectively controlled within the satisfied range.

To improve the control performance of the DC-link voltage regulation against the load disturbance, a lead compensator is proposed in [37] to regulate the DC-link voltage reference when the voltage error exceeds a certain value. A feed-forward compensator is proposed in [38] to reduce the DC-link voltage fluctuation when the load changes. However, the compensator performance is only validated using a step load change but its performance under various drive cycles is unknown. In [36], a feed-forward load compensator is proposed and verified by various drive cycles, but the performance of the compensator is dependent on several parameters and the complexity is increased. Also, the load disturbance current is assumed to be measurable. However, under such cases that there exists the measurement error in the load current or the load current cannot be measured, the performance of the compensator deteriorates or even unachievable.

As aforementioned, the adaptive frequency control is widely used in battery/supercapacitor hybrid energy storage system, but its application in FC/SC hybrid system is different and the cut-off frequency should be adaptively controlled by the FC current, SC voltage and the drive cycle current. The reason is that the FC characteristics are significantly different from that of the battery. First, the FC can only provide the power but cannot absorb the regenerative power, while the battery has the bidirectional power flow; Second, the FC voltage decreases with the increase of the current and the FC output voltage is highly dependent on its load current while the battery voltage mainly varies with its SoC level; Third, the FC has slower dynamics than that of the battery due to the internal chemical reactions. Therefore, the control strategy in the FC/SC hybrid powertrain should be developed with considerations of the FC output characteristics and the control strategy in the battery/supercapacitor system cannot be applied in the FC/SC hybrid system directly.

This work is motivated by [36] and developed on [39], where the same topic is addressed including the adaptive power split strategy and the improvement of the DC-link voltage regulation against the load disturbance. The feasibility of the method proposed in [36] is validated using simulations in FC/SC hybrid powertrain [39]. The simulations show that the load cut-off frequency can be changed adaptively based on the SC SoC while the DC bus voltage variation is reduced by the load disturbance compensator. This paper is a continuation work of [39] and further demonstrates the effectiveness of the adaptive power split and the load disturbance compensator by performing extensive experiments. Two original contributions are delivered in the paper. First, to improve the FC performance and maintain a reasonable SC SoC level, the cut-off frequency is adaptively adjusted with consideration of the FC load characteristics and the SC SoC level; Second, to achieve a better tracking performance and the anti-disturbance (load current) of the DC-link voltage control, a feed-forward compensator is applied with a load disturbance observer to estimate the load current, which is also applicable in cases where the load current is not measurable, or measurement error exists.

The remainder of this paper is organized as follows. Section 2 describes the system architecture and component models of a hybrid FC/SC electric vehicle. Section 3 presents the control strategy. Section 4 shows the experimental results. Section 5 concludes this paper.

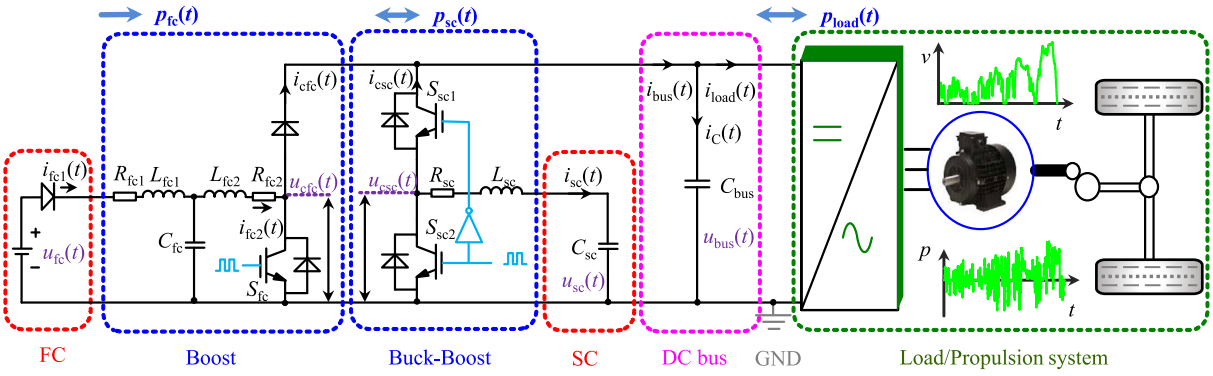


**Fig. 1.** A hybrid FC/SC system for electric vehicle applications..

## 2. System architecture and component modeling

The system architecture of a hybrid FC/SC electric vehicle is shown in Fig. 1 and the variables in the time-domain are marked as small letters, while capital letters are used in frequency-domain. The FC and the SC are represented by a voltage source, $u_{fc}(t)$, and a capacitor, $C_{sc}$, respectively. The load profile, $p_{load}(t)$, is obtained from the speed profile. The controller for the SC buck–boost converter is designed to be faster than the controller for the FC boost converter to make sure that the FC does not respond to the sudden load current variation but gradually ramps up to follow the reference. The FC and SC converters share the same DC bus capacitor $C_{bus}$. Therefore, their output voltages are always the same.

The propulsion system including a DC/AC inverter, an electric machine, a transmission, and wheels is treated as the dynamic load of the FC/SC hybrid system. When the vehicle operates in the acceleration mode, power flows from the hybrid system to the propulsion system. In the deceleration mode, power flows in the opposite direction. As shown in Fig. 1, $p_{load}(t)$ is the power transferred between the hybrid system and the propulsion system. The power balance equations at the DC-bus side can be expressed as

$$p_{load}(t) = p_{fc}(t)\eta_{boost} + p_{sc}(t)\eta_{buck\text{-}boost}^{-sign(p_{sc}(t))}, \quad (1)$$

where $\eta_{boost}$ and $\eta_{buck\text{-}boost}$ are the efficiencies of the boost converter and buck–boost converter, respectively. The function "sign" allows the efficiency of the buck–boost converter to be shifted according to the direction of the SC power flow.

### 2.1. Boost converter for fuel cell

A typical voltage of an individual FC cell is low and variable with respect to the load current and several cells are connected in series to form a FC stack to get a certain voltage. The polarization curve of the FC stack used in our case is shown in Fig. 2, illustrating a decreased voltage along with the increase of the current. During the FC operation, the hydrogen gas and oxygen gas cannot respond to the load current changes instantaneously and FC should be operated steadily at the determined combination of voltage and current to make FC work efficiently. Usually, a boost converter is needed to convert the FC voltage and control its dynamics. As shown in Fig. 1, the inductor $L_{fc1}$ and the capacitor $C_{fc}$ act as the input filter for the boost converter. $L_{fc2}$ is the input inductor of the boost converter. $R_{fc1}$ and $R_{fc2}$ are the parasitic resistors of $L_{fc1}$ and $L_{fc2}$, respectively.

This paper adopts the average model and neglects the losses of power electronics. The average voltage across the switch $S_{fc}$ is denoted as $U_{cfc} = D'_{fc}U_{bus}$, where $D'_{fc} = 1 - D_{fc}$ and $D_{fc}$ is the duty ratio of the gate signal for the FC side of the boost converter. Therefore, the high-frequency switching ripples can be neglected. The input current of the

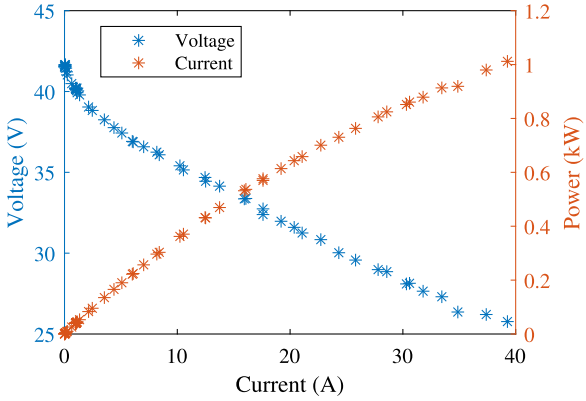


**Fig. 2.** Operation curve of Nexa 1.2 kW fuel cell stack with a total of 47 cells connected in series and more detailed parameters are given in [40].

boost converter is derived as given in Box I. A variable change is introduced as

$$U_{mfc}(s) = \frac{U_{fc}(s)}{L_{fc1}C_{fc}s^2 + R_{fc1}C_{fc}s + 1} - U_{cfc}(s), \quad (3)$$

which can be used to limit the inrush current when the converter starts since the variable change is set as 0 and FC voltage equals to switch voltage. The inductor current changes slowly from 0 due to the second-order system.

The converter transfer function can be derived as (4) using the framework in [41,42]. The converter model is a third-order system and it can be approximated as a first-order system because the coefficients for the cubic and quadratic terms are sufficiently small and can be neglected. The Bode plots of the original transfer function model and the simplified one are shown in Fig. 3 and the effect of the capacitance variation is also depicted. The capacitor $C_{fc}$ of the input filter indeed can be neglected at low frequency since the FC has quite slow dynamics. The amplitude–frequency characteristics and phase–frequency characteristics of the simplified transfer function show almost the same performance with the original one even when the capacitance of $C_{fc}$ varies with ±20% of the nominal value. The controller for this converter is designed based on this first-order model using the method in [34]. With the first-order approximated model, the current of inductor $L_{fc1}$ is the same as that of inductor $L_{fc2}$ with the denotation of $I_{fc1} = I_{fc2} = I_{fc}$ (see Box II).

### 2.2. Buck–boost converter for supercapacitor

A bidirectional DC/DC converter is used to discharge and charge the SC. The gate signals for $S_{sc1}$ and $S_{sc2}$ are always complementary with a small dead-time inserted. $L_{sc}$ is the output inductor and $R_{sc}$ is

$$I_{\mathrm{fc2}}(s)=\frac{U_{\mathrm{fc}}(s)-\left(L_{\mathrm{fc1}}C_{\mathrm{fc}}s^2+C_{\mathrm{fc}}R_{\mathrm{fc1}}s+1\right)U_{\mathrm{cfc}}(s)}{L_{\mathrm{fc1}}L_{\mathrm{fc2}}C_{\mathrm{fc}}s^3+C_{\mathrm{fc}}\left(L_{\mathrm{fc1}}R_{\mathrm{fc2}}+L_{\mathrm{fc2}}R_{\mathrm{fc1}}\right)s^2+\left(C_{\mathrm{fc}}R_{\mathrm{fc1}}R_{\mathrm{fc2}}+L_{\mathrm{fc1}}+L_{\mathrm{fc2}}\right)s+\left(R_{\mathrm{fc1}}+R_{\mathrm{fc2}}\right)}. \tag{2}$$

**Box I.**

$$\begin{aligned}G_{\mathrm{fc}}(s)&=\frac{I_{\mathrm{fc}}(s)}{U_{mfc}(s)},\\&=\frac{C_{\mathrm{fc}}L_{\mathrm{fc1}}s^2+C_{\mathrm{fc}}R_{\mathrm{fc1}}s+1}{L_{\mathrm{fc1}}L_{\mathrm{fc2}}C_{\mathrm{fc}}s^3+C_{\mathrm{fc}}\left(L_{\mathrm{fc1}}R_{\mathrm{fc2}}+L_{\mathrm{fc2}}R_{\mathrm{fc1}}\right)s^2+\left(C_{\mathrm{fc}}R_{\mathrm{fc1}}R_{\mathrm{fc2}}+L_{\mathrm{fc1}}+L_{\mathrm{fc2}}\right)s+\left(R_{\mathrm{fc1}}+R_{\mathrm{fc2}}\right)},\\&\approx\frac{1}{sL_{\mathrm{fc}}+R_{\mathrm{fc}}},\end{aligned} \tag{4}$$

where $L_{\mathrm{fc}}=L_{\mathrm{fc1}}+L_{\mathrm{fc2}}$, $R_{\mathrm{fc}}=R_{\mathrm{fc1}}+R_{\mathrm{fc2}}$.

**Box II.**

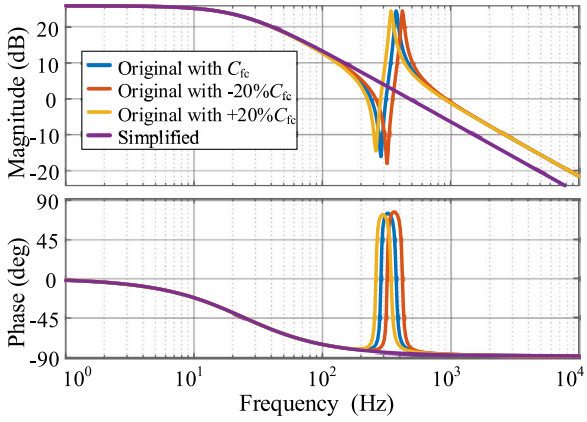


**Fig. 3.** Bode plots of the transfer function of the boost converter, including the original one with capacitance variations and the simplified one. All curves are obtained from Eq. (4) with the first three curves showing the influence of the capacitance $C_{\mathrm{fc}}$ variation on the original transfer function and the last one indicating the simplified one.

the parasitic resistor. The average voltage across $S_{\mathrm{sc2}}$ is denoted as $U_{\mathrm{csc}}$ and the high order switching ripples are neglected. The SC current can be derived as

$$I_{\mathrm{sc}}(s)=\frac{U_{\mathrm{csc}}(s)-U_{\mathrm{sc}}(s)}{sL_{\mathrm{sc}}+R_{\mathrm{sc}}}. \tag{5}$$

Similar to (3), a variable change is defined as

$$U_{msc}(s)=U_{\mathrm{csc}}(s)-U_{\mathrm{sc}}(s). \tag{6}$$

Therefore, the transfer function of the converter is written as

$$G_{\mathrm{sc}}(s)=\frac{I_{\mathrm{sc}}(s)}{U_{msc}(s)}=\frac{1}{sL_{\mathrm{sc}}+R_{\mathrm{sc}}}. \tag{7}$$

This converter model is a first-order system and its controller is designed accordingly.

### 2.3. Current loop model

Based on (4) and (7), it can be observed that the FC and SC converter models show the same first-order linear time-invariant system structure, which can be rewritten as

$$G_{xx}(s)=\frac{I_{xx}(s)}{U_{mxx}(s)}=\frac{1}{sL_{xx}+R_{xx}},\ xx=\text{fc or sc}. \tag{8}$$

The transfer function, $G_{xx}(s)$, can be controlled by the PI controller and the closed-loop transfer function can be described as

$$G_{\mathrm{cl\_}xx}(s)=\frac{G_{\mathrm{PI}xx}(s)G_{xx}(s)}{1+G_{\mathrm{PI}xx}(s)G_{xx}(s)}=\frac{T_{\mathrm{i}xx}s+1}{T_{0xx}^2s^2+2\xi_{xx}T_{0xx}s+1}, \tag{9}$$

with $G_{\mathrm{PI}xx}(s)=K_{\mathrm{p}xx}+\frac{K_{\mathrm{i}xx}}{s}$, where $K_{\mathrm{p}xx}$ and $K_{\mathrm{i}xx}$ respectively denote the coefficients of proportional and integral gains in the PI controller with the time constant calculated as $T_{\mathrm{i}xx}=K_{\mathrm{p}xx}/K_{\mathrm{i}xx}$. $T_{0xx}$ and $\xi_{xx}$ are the time constant and damping coefficient, which is respectively identified as

$$\begin{cases}T_{0xx}=\sqrt{\dfrac{T_{\mathrm{i}xx}T_{\mathrm{f}xx}}{K_{\mathrm{p}xx}K_{\mathrm{f}xx}}},\\ \xi_{xx}=\dfrac{T_{\mathrm{i}xx}}{2T_{0xx}}\left(1+\dfrac{1}{K_{\mathrm{p}xx}K_{\mathrm{f}xx}}\right),\end{cases} \tag{10}$$

where $T_{\mathrm{f}xx}=L_{xx}/R_{xx}$ and $K_{\mathrm{f}xx}=1/R_{xx}$.

Considering the actual parameter values of the current PI controllers, it can be observed that $T_{0xx}^2\approx 0$ and $2\xi_{xx}T_{0xx}\approx T_{\mathrm{i}xx}$. Therefore, the closed-loop transfer functions of the current loop are approximately equal to 1 in the low-frequency range.

A low-pass filter (LPF) shown in (11) is used to split the DC bus reference current into two parts due to the intrinsic characteristics of the FC and the SC. The low-frequency component is supplied by the FC and the high-frequency part is going to the SC. In case of negative current and large current change rate, a saturation block and a ramp limiter are designed for the FC reference current. Current regulation of the FC and SC is realized by their respective converter as mentioned before.

$$H_{\mathrm{LPF}}(s)=\frac{1}{T_{\mathrm{i}}\cdot s+1}, \tag{11}$$

where $T_{\mathrm{i}}=1/(2\pi f_{\mathrm{c}})$ with $f_{\mathrm{c}}$ being the cut-off frequency. Therefore, the closed-loop transfer function of the DC bus current control including the low-pass filter can be derived as

$$G_{\mathrm{cur}}(s)=H_{\mathrm{LPF}}(s)G_{\mathrm{cl\_fc}}(s)+(1-H_{\mathrm{LPF}}(s))G_{\mathrm{cl\_sc}}(s). \tag{12}$$

### 2.4. DC bus model

The boost and buck–boost converters share the same DC bus capacitor. Using Kirchhoff's current law, one can get

$$\begin{aligned}C_{\mathrm{bus}}\frac{\mathrm{d}u_{\mathrm{bus}}(t)}{\mathrm{d}t}&=i_{\mathrm{bus}}(t)-i_{\mathrm{load}}(t),\\&=i_{\mathrm{cfc}}(t)+i_{\mathrm{csc}}(t)-i_{\mathrm{load}}(t).\end{aligned} \tag{13}$$

The load current can be regarded as a disturbance. The transfer function from the DC bus current and the load disturbance current to the DC bus voltage can be respectively derived as

$$\begin{cases} G_{\text{bus}}(s) = \dfrac{U_{\text{bus}}(s)}{I_{\text{bus}}(s)} = \dfrac{1}{sC_{\text{bus}}}, \\ G_{\text{load}}(s) = \dfrac{U_{\text{bus}}(s)}{I_{\text{load}}(s)} = -\dfrac{1}{sC_{\text{bus}}}. \end{cases} \tag{14}$$

The voltage PI controller can also be designed and the closed-loop transfer function of the DC bus voltage control can be derived as

$$G_{\text{vol}}(s) = \frac{G_{\text{PI}}(s)G_{\text{cur}}(s)G_{\text{bus}}(s)}{1 + G_{\text{PI}}(s)G_{\text{cur}}(s)G_{\text{bus}}(s)}. \tag{15}$$

### 2.5. Dynamic load model

The propulsion system acts as the dynamic load, which is a controlled bidirectional current source calculated based on the power required during the vehicle operation. The required power is determined using the vehicle dynamics [43–45]

$$\begin{aligned} p_{\text{load}}(t) &= F_{\text{wheel}}(t)v(t)\eta^{-\text{sign}(F_{\text{wheel}}(t))} \\ &= \left(\frac{\rho_a C_d A_f v(t)^2}{2} + C_r mg\cos\alpha(t) + (m+m_r)\frac{dv(t)}{dt} + mg\sin\alpha(t)\right) \\ &\quad \times v(t)\eta^{-\text{sign}(F_{\text{wheel}}(t))}, \end{aligned} \tag{16}$$

where $F_{\text{wheel}}(t)$ is the traction force applied to wheels, $v(t)$ is the vehicle speed, and $\eta$ is the energy conversion efficiency of the propulsion system, including the electric machine and the associated three-phase inverter. $\rho_a$ is the air density, $C_d$ is the aerodynamic drag coefficient, and $A_f$ is the front area. $C_r$ is the rolling resistance coefficient, $m$ is the vehicle mass, $g$ is the gravitational acceleration, and $\alpha$ is the road slope. $m_r$ is the equivalent mass of the rotating parts and can be calculated by the inertia of the electric machine and the wheels. The term $m_r$ is usually supposed to be 0 for simplification purposes in the case study.

Under a given drive cycle, the power demand of the vehicle can be calculated. In this case study, the power level of the experimental setup is significantly lower than that of the real vehicle. Hence, the calculated power from (16) is scaled down by a zoom multiplier $k$, the down-scaled controlled current source can be written as

$$i_{\text{load}}(t) = \frac{p_{\text{load}}(t)}{k u_{\text{bus,ref}}}. \tag{17}$$

In summary, the component model parameters are listed in Table 1.

## 3. Control framework for FC/SC hybrid system

The proposed control framework for the FC/SC hybrid system is illustrated in Fig. 4, which features an adaptive power split strategy and a load disturbance compensator. The target of the adaptive power split strategy is to generate an adaptive cut-off frequency adjusted by the load current and the SC SoC and the load disturbance compensator is to estimate the load current and counteract its effect on the DC-bus voltage.

### 3.1. Fixed power splitting

To illustrate the necessity of the adaptive power split, simulations are conducted with cut-off frequencies of 0.01, 0.04, and 0.08 Hz for four drive cycles, including Artemis Urban, WLTC, US06 and HWFET and results are shown in Fig. 5. To make fair comparisons, the same initial SC SoC and load current are set for all cases. Also, a saturation block and a rate limiter are applied to the FC current to avoid the negative current and the large current variation.

**Table 1**
Component model parameters.

| Module | Parameter | Value |
|---|---|---|
| Fuel cell | Rated power (kW) | 1.2 |
| | Rated voltage (V) | 26 |
| Supercapacitor | Rated capacitance (F) | 165 |
| | Rated voltage (V) | 48 |
| DC/DC converter | $V_{\text{bus,ref}}$ (V) | 75 |
| | Switching frequency (kHz) | 20 |
| | DC bus capacitor $C_{\text{bus}}$ (F) | $2.7\times10^{-3}$ |
| | Capacitor $C_{\text{fc}}$ (F) | $2.2\times10^{-3}$ |
| | Inductor $L_{\text{fc1}}$ (H) | $140\times10^{-6}$ |
| | Inductor $L_{\text{fc2}}$ (H) | $191.3\times10^{-6}$ |
| | Inductor $L_{\text{sc}}$ (H) | $34.4\times10^{-6}$ |
| | Parasitic resistor $R_{\text{fc1}}$ ($\Omega$) | 0.01 |
| | Parasitic resistor $R_{\text{fc2}}$ ($\Omega$) | 0.04 |
| | Parasitic resistor $R_{\text{sc}}$ ($\Omega$) | 0.04 |
| | $K_{\text{p}}$ DC-link voltage controller (-) | 11.4 |
| | $K_{\text{i}}$ DC-link voltage controller(-) | 227 |
| | $K_{\text{pfc}}$ FC current controller (-) | 0.014204 |
| | $K_{\text{ifc}}$ FC current controller (-) | 16.3208 |
| | $K_{\text{psc}}$ SC current controller (-) | 0.1337 |
| | $K_{\text{isc}}$ SC current controller (-) | 112.1042 |

It can be seen that under Artemis Urban drive cycle, the SC SoC is almost balanced when the cut-off frequency is 0.01 Hz, while the SC SoC increases from 70.5% to 80% and 84% under the frequency of 0.04 and 0.08 Hz, respectively. SC will experience over-charging when the drive cycle continues. For the WLTC drive cycle, the SC SoC increases slightly higher than that of Artemis Urban drive cycle while the SC SoC increase slightly lower under HWFET drive cycle. When the US06 drive cycle is applied, the SC has a deep discharge under the cut-off frequency of 0.01 and 0.04 Hz, and over-charge under all cut-off frequencies. It is obvious that the fixed cut-off frequency cannot be applicable for all driving cycles and a varied cut-off frequency is required.

### 3.2. Adaptive power split strategy

Due to the inability to recover the regenerative braking energy of FC, the SC takes over all regenerative power when the load current is negative. Also, the FC is assumed to have a minimum operation power to reduce the FC degradation caused by zero load current. The SC is also charged by the FC during the regenerative braking mode. During the propulsion mode, the load current needs to be properly allocated. To adaptively split the low and high-frequency portions of the load current, the artificial potential field method [36] is adopted. The virtual attractive force is defined as a function of the SC SoC during propulsion mode. The power allocation ratio is derived from the virtual attractive force to decide the cut-off frequency adaptively by cutting the load frequency spectrum. Therefore, the power provided by the SC is dependent on its SoC level and the load power. The SC undertakes more propulsion power at a higher SoC level, while less propulsion power at a lower SoC level.

The virtual attractive force varying with the SC SoC level is defined as

$$F_{\text{sc}}(x) = \begin{cases} \text{sign}(x)\dfrac{20^{|ax|}-1}{20^{|a(\text{SoC}_{\max}-\text{SoC}_{\text{mid}})|}-1}, x \geq 0. \\ \text{sign}(x)\dfrac{20^{|ax|}-1}{20^{|a(\text{SoC}_{\text{mid}}-\text{SoC}_{\min})|}-1}, x < 0, \end{cases} \tag{18}$$

where $F_{\text{sc}}$ is the virtual attractive force and $a$ is the coefficient that influences the slope of the virtual attractive force $F_{\text{sc}}$. $\text{SoC}_{\min}$ and $\text{SoC}_{\max}$ are the minimum and maximum SoC level, respectively, which are normalized by $x = \text{SoC} - \text{SoC}_{\text{mid}}$ with $\text{SoC}_{\text{mid}}$ being a value between $\text{SoC}_{\min}$ and $\text{SoC}_{\max}$. $\text{SoC}_{\text{mid}}$ is an adjustable parameter and it will determine the variation trend of the virtual attractive force at higher SoC level and lower SoC level. When $\text{SoC}_{\text{mid}}$ is the midpoint

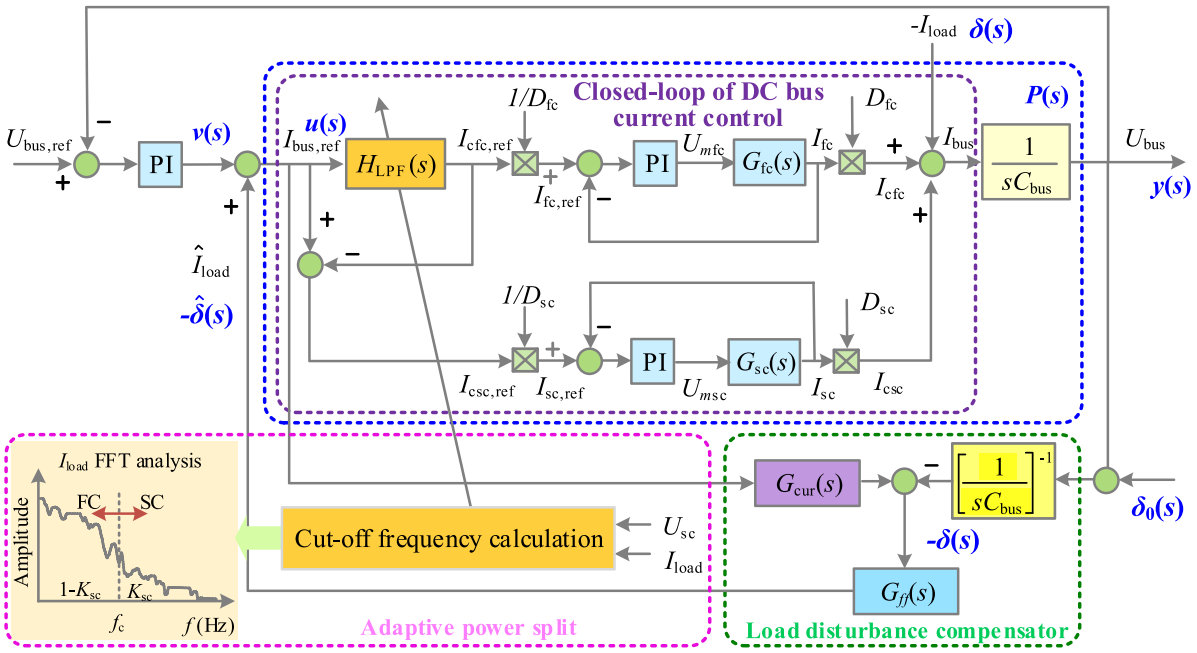


**Fig. 4.** Control framework of FC/SC hybrid system.

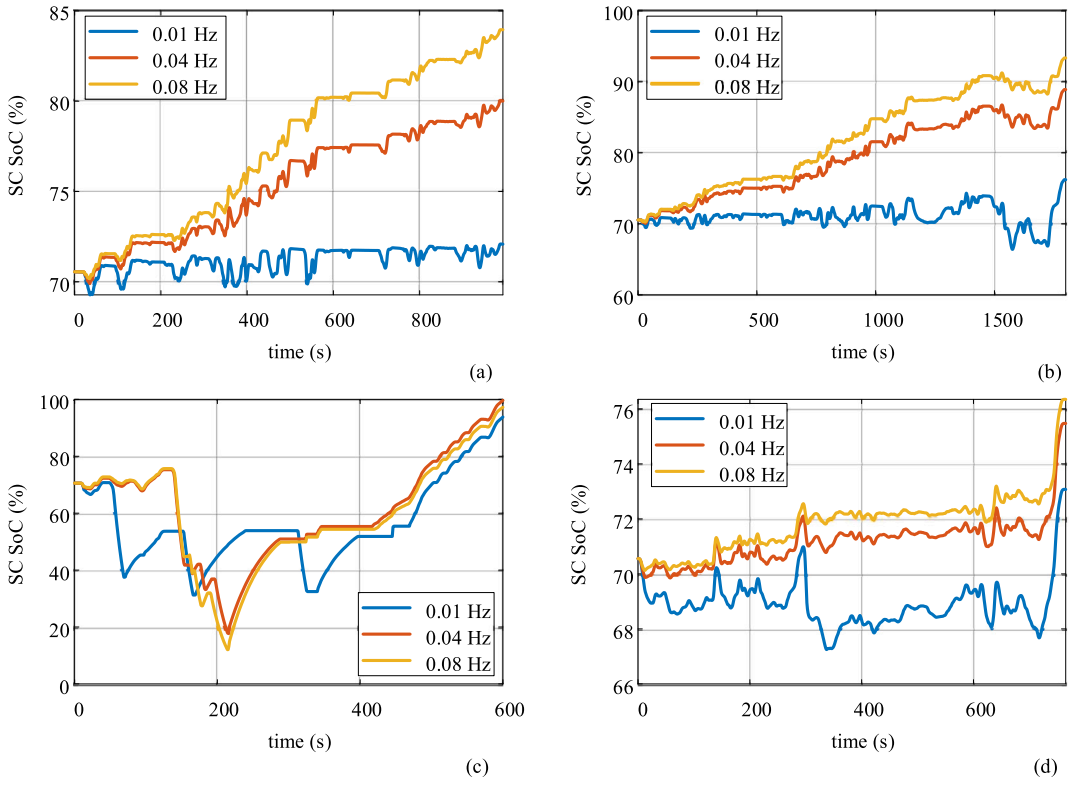


**Fig. 5.** SC SoC under the cut-off frequency of 0.01 Hz, 0.04 Hz and 0.08 Hz. (a) Artemis Urban; (b) WLTC; (c) US06; (d) HWFET.

of the selected SoC range, the virtual attractive force is symmetric; otherwise, the virtual attractive force is asymmetric. The asymmetric virtual attractive forces when $a = 1, 5, 20$ are shown in Fig. 6, where $SoC_{mid}$ is selected as 0.55 with the SoC range varying from 0.3 to 0.9.

A discrete fast Fourier transform (FFT) is performed on $N$ samples of the load current $I_{load}$ and the frequency spectrum is obtained as

$$I_{load}(k) = \sum_{n=1}^{N} i_{load}(n) W_N^{(n-1)(k-1)}, \tag{19}$$

where $W_N = e^{-2\pi j/N}$ is one of $N$ roots of unity and $N$ is the FFT length.

Due to the unidirectional power flow of the FC, a minimum cut-off frequency is directly set as its maximum in the low-pass filter $H_{LPF}(s)$ when the load current is negative, while the cut-off frequency is adaptively controlled by the area ratio in the frequency spectrum of the load current when the load current is positive. The area ratio, $K_{sc}$, is defined as the high-frequency spectrum area over the total frequency spectrum area [35]. Once $K_{sc}$ is determined, the cut-off frequency $f_c$ can be calculated. The relationship between $K_{sc}$ and $F_{sc}$ during

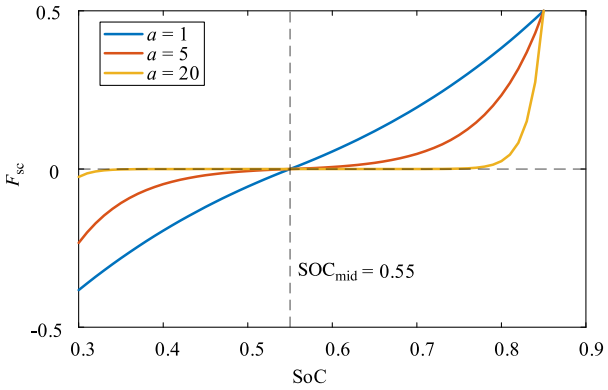


**Fig. 6.** Virtual attractive force with SC SoC during propulsion mode.

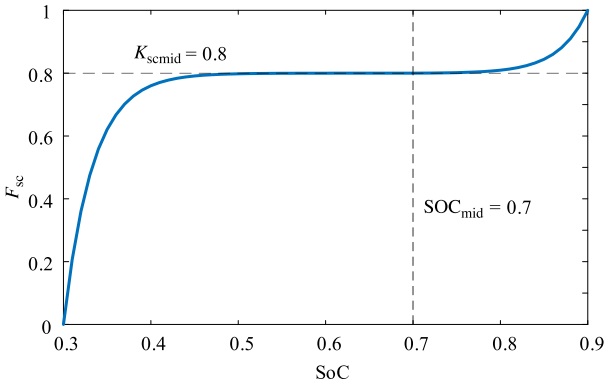


**Fig. 7.** Illustration of the artificial potential field during propulsion mode.

propulsion mode can be written as

$$K_{sc}(F_{sc}) = \left[0.5 + \text{sign}\left(-F_{sc}\right)\left(K_{scmid} - 0.5\right)\right] F_{sc} + K_{scmid}, \tag{20}$$

where $K_{scmid}$ is an adjustable parameter, which determines the load power allocated to the SC in the region around the $SoC_{mid}$. Once the virtual attractive force $F_{sc}$ is obtained, the area ratio $K_{sc}$ can be calculated according to (20). The artificial potential field with $a = 10$, $SoC_{mid} = 0.7$, $K_{scmid} = 0.8$ as an example is shown in Fig. 7. Note that $K_{sc}$ should be bounded between 0 and 1. During propulsion mode, $K_{sc}$ is smaller when the SoC level is low and it is bigger when the SoC level is high. This means that the SC supplies more load power at a higher SoC level and less load power at a lower SoC level.

The implementation of the adaptive power split strategy is described in Fig. 8.

### 3.3. Load disturbance compensator

In the cascaded PI control, the load current disturbance is acted at the outside of the inner current loop control, and the anti-load disturbance effect can only be achieved by the outer voltage loop control. However, the load disturbance is assumed to be 0 or a constant value when the voltage PI controller is designed. Therefore, the control performance is degraded when the disturbance is a time-variant signal or the parameters change. To improve the control performance of the DC bus voltage regulation, a feed-forward controller is needed to compensate the effect of the load disturbance on the system output. A simplified block diagram of the control framework is shown in Fig. 9 to highlight the load disturbance compensator. $\delta(s)$ is the inverse of the load current, which is the system disturbance and has effects of $G_{bus}(s)$ on the system output $y(s)$. Therefore, the main task of the load disturbance compensator is to estimate the load current and compensate this current to the input $v(s)$.

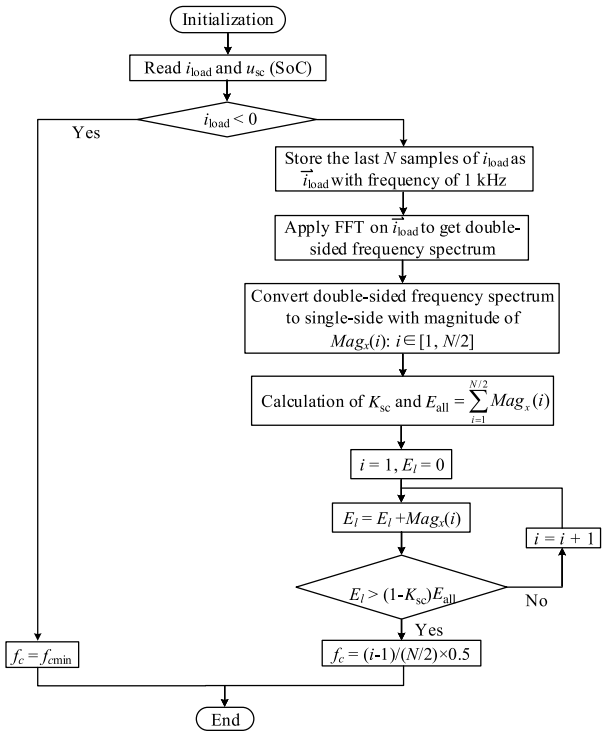


**Fig. 8.** Flow chart of the implementation of the adaptive power split.

The control plant of the DC bus voltage can be written as $P(s) := P_n(s) + \Delta(s)$ with the nominal dynamics $P_n(s)$ used for controller design and the uncertain dynamics $\Delta(s)$. In which, $P_n(s) = G_{cur}(s)G_{bus}(s)$. $Q(s)$ is the Butterworth low-pass filter with a relative degree greater or equal to that of $P_n(s)$. $\delta_0(s)$ is sensor noise. The load current disturbance can be estimated with a linear function of the system input $u(s)$ and the output $y(s)$,

$$\hat{\delta}(s) = Q(s)\left(u(s) - P_n^{-1}(s)y(s) - P_n^{-1}(s)\delta_0(s)\right), \tag{21}$$

and the closed-loop transfer function from $v(s)$ to $y(s)$ then becomes,

$$H_{LDC}(s) = \frac{P(s)}{1 + Q(s)\left(P(s)P_n(s)^{-1}(s) - 1\right)}, \tag{22}$$

we can see that for low frequencies where $Q(s) \approx 1$ and $H_{LDC} \approx P_n(s)$, which means that the load disturbance compensator can make the system perform the same behavior as the nominal plant model. One can get $y \approx P_n v - \delta_0$ and the system output $y(s)$ can track the reference $v(s)$ without the influence of the disturbance $\delta'(s)$, where $\delta'(s) = \delta(s)/G_{cur}(s)$. Furthermore, the plant is the same as the nominal plant model ($P(s) = P_n(s)$) when $\Delta(s) \equiv 0$, then $\hat{\delta} = 0$ and the load disturbance compensator does not change the plant behavior. It should be noted that the performance of the load disturbance compensator is closely related to the design of the $Q(s)$ filter and more details can be found in [46].

### 3.4. Stability and robustness

#### 3.4.1. Stability analysis

Since FC current controller is designed to be slower than that of the SC, and also a low-pass filter is applied to the FC current, the dynamics of the closed-loop transfer function of the DC bus current control as shown in (12) is mainly determined by the SC current control loop. Therefore, $G_{cur}(s)$ can be approximated as a first-order system. In this way, the effect of the time constant variation in the low-pass filter can

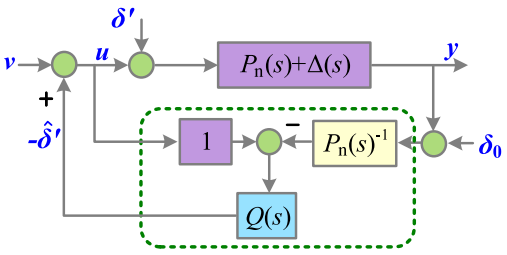


**Fig. 9.** Illustration of the load disturbance compensator.

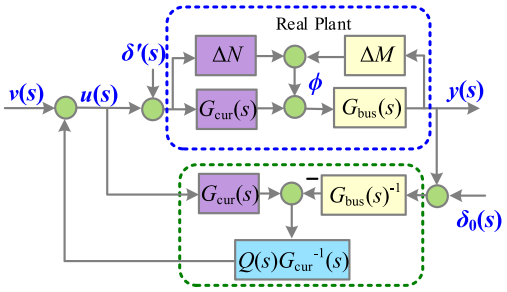


**Fig. 10.** Load disturbance compensator with uncertainties.

be canceled. Hence, the closed-loop transfer function of the DC bus voltage control is derived as

$$G_{vol}(s) = \frac{588.3s + 4.933 \times 10^5}{0.00272s^3 + 11.97s^2 + 588.3s + 4.933 \times 10^5}, \tag{23}$$

we can clearly see that the poles of the transfer function $G_{vol}(s)$ is located at the left half of the $s$-plane, so the closed-loop system is stable.

### 3.4.2. Robustness analysis

With consideration of perturbation $\Delta M$ and $\Delta N$, the system is shown in Fig. 10. The perturbation quantity can be expressed as

$$\phi = \begin{bmatrix} \Delta M & \Delta N \end{bmatrix} \begin{bmatrix} y \\ u + \delta' \end{bmatrix}, \tag{24}$$

and assume that bound on the uncertainties is expressed as

$$\left\| \begin{bmatrix} \Delta M & \Delta N \end{bmatrix} \right\|_\infty < \frac{1}{\gamma}, \tag{25}$$

where $\gamma$ is the uncertainty bound. We can also get another relation from Fig. 10, as follows

$$\begin{bmatrix} y \\ u + \delta' \end{bmatrix} = \begin{bmatrix} P_n \\ 1 \end{bmatrix} v + \begin{bmatrix} (1-Q)G_{bus} \\ -QG_{cur}^{-1} \end{bmatrix} \phi + \begin{bmatrix} (1-Q)P_n \\ (1-Q) \end{bmatrix} \delta' - \begin{bmatrix} Q \\ QP_n^{-1} \end{bmatrix} \delta_0. \tag{26}$$

The small gain theorem is applied to (24) and (26) and the robustness bound of the load disturbance compensator can be obtained as

$$\left\| \begin{bmatrix} (1-Q)G_{bus} \\ -QG_{cur}^{-1} \end{bmatrix} \right\|_\infty < \gamma, \tag{27}$$

Multiply both sides of (27) by $\begin{bmatrix} G_{bus}^{-1} & G_{cur} \end{bmatrix}$, the degree of robustness of the load disturbance compensator against the perturbation can be shown as

$$\sigma_{max} \triangleq \left\| \begin{bmatrix} (1-Q) & (1-Q)P_n \\ -QP_n^{-1} & -Q \end{bmatrix} \right\|_\infty < \gamma, \tag{28}$$

We can see that if a small $\sigma_{max}$ is achieved by designing an adequate $Q(s)$ for a given nominal plant $P_n(s)$, the load disturbance compensator can make the system stabilize despite the large perturbation or uncertainties. The robustness against the perturbation or uncertainties is closely related to the parameters of $Q$ filter. More detailed information on filter design can be found in [47].

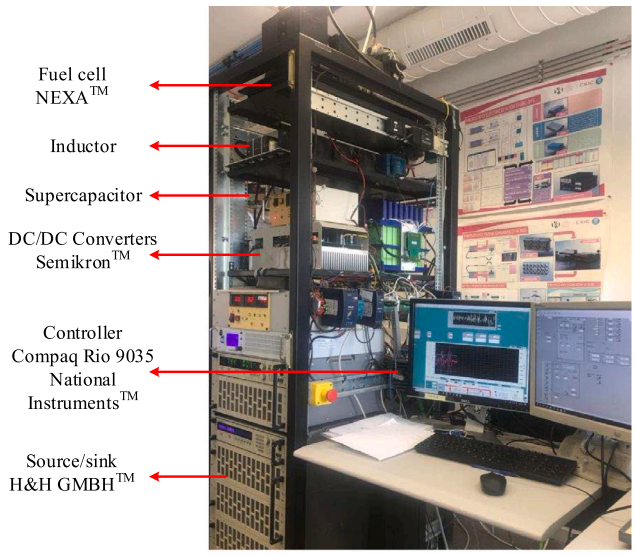


**Fig. 11.** Experimental setup for FC/SC hybrid system.

## 4. Experiments and results

### 4.1. Experimental setup

The experimental work was carried out in the IRI fuel cell laboratory (UPC-CSIC) in Barcelona (Spain) using the test station shown in Fig. 11. The demand load current profile is precalculated using (16) and (17), which is simulated by the Höcherl & Hackl NL series programmable current source/sink. The control strategy is implemented in FPGA (CompactRIO from NI) using LabVIEW. The data required for the controller is acquired from voltage and current sensors using NI 9201 C series voltage input modules.

### 4.2. Validation of load disturbance compensator

#### 4.2.1. Short-term scenario

The performance of the load disturbance compensator is first validated by a step load current, which is denoted as the short-term scenario. The results are shown in Fig. 12. The load current first increases from 0 to 5 A with various steps (e.g., 2 A at 16 s) and then decreases to 0 A. These changes result in changes in the instantaneous power (e.g., 150 to 225 W at 51 s).

To limit the FC power variation and maintain a reasonable SC SoC level, the cut-off frequency should be properly selected. A cut-off frequency of 0.04 Hz is suitable for our particular case for comparison, and a same cut-off frequency is set for the control schemes with and without the load disturbance compensator. According to (14), the effect of the load current disturbance to the output voltage is described by the transfer function $-\frac{1}{s}C_{bus}$. This effect is designed to be rejected by the voltage control loop in the conventional cascaded PI control. Since the voltage PI control loop is 10 times slower than the current inner PI loop. There is always a voltage lag in the DC bus voltage regulation due to the error-based PI controller. As shown in Fig. 12(c), when the load current steps up from 3 to 5 A at 74 s, the DC bus voltage instantaneously drops from 75 to 73.2 V. Without the load disturbance compensator, it takes 0.5 s for the DC bus voltage to recover to the reference voltage. On the other hand, the DC bus voltage remains almost unchanged when the load disturbance compensator is introduced. As another example, when the load current steps down from 5 to 2 A at 103.2 s, the DC bus voltage has an overshoot of 2.5 V without the load disturbance compensator. For comparison, the overshoot is significantly reduced to around ±0.2 V when the load disturbance compensator is in place.

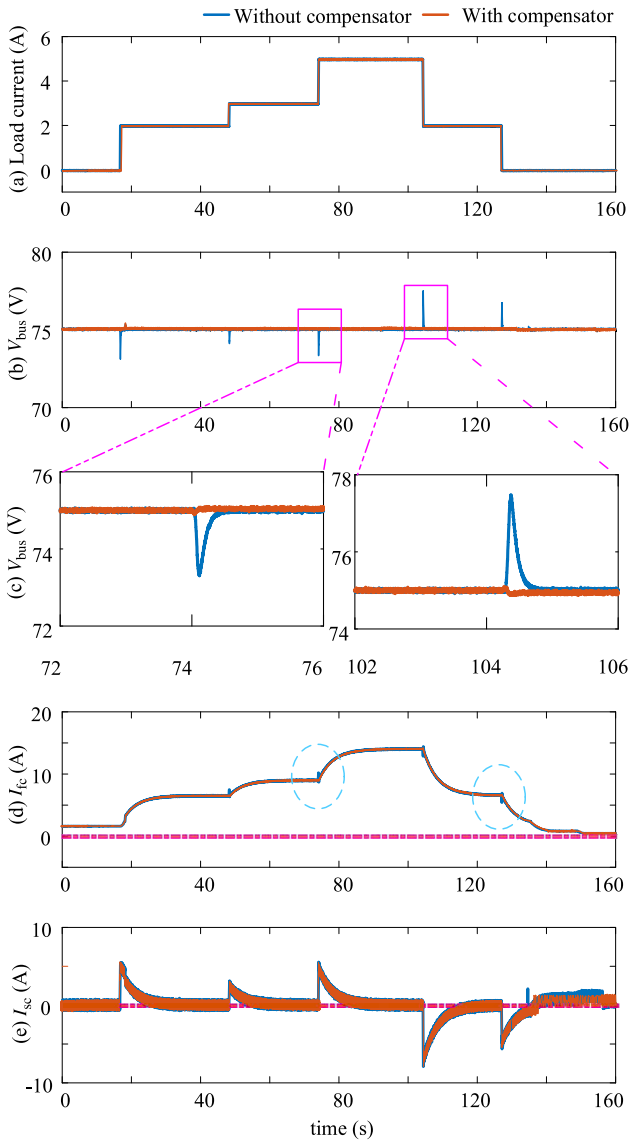


**Fig. 12.** Experimental results for step load current: with and without load disturbance compensator, $f_c$ = 0.04 Hz. Blue plots show the results without load disturbance compensator and red plots show the result with load disturbance compensator. The magenta straight lines in (d) and (e) indicate 0 A. (a) Load current; (b) DC bus voltage; (c) DC bus voltage for [72, 76] s and [102, 106] s; (d) Fuel cell current; (e) Supercapacitor current.

It should be noted that due to the DC bus voltage variations resulted by the sudden load current changes, the FC current experiences overshoots or dips when the load disturbance compensator is not in use. For example, there is a 1 A overshoot when the load current steps up at 74 s and a 1 A dip when the load current steps down at 124 s, which are marked in the blue dotted circles in Fig. 12(d). In contrast, the FC current becomes smoother when the load disturbance compensator is introduced.

#### 4.2.2. Long-term scenario

The standard WLTC drive cycle is used to verify the performance of the load disturbance compensator in a long-term scenario. The experimental results under a constant cut-off frequency of 0.04 Hz are compared in Fig. 13. Due to the frequent acceleration and deceleration of the electric vehicle, the load power varies accordingly and causes large variations of the load current. As shown in Fig. 13(b), the DC bus voltage fluctuates a lot without the load disturbance compensator.

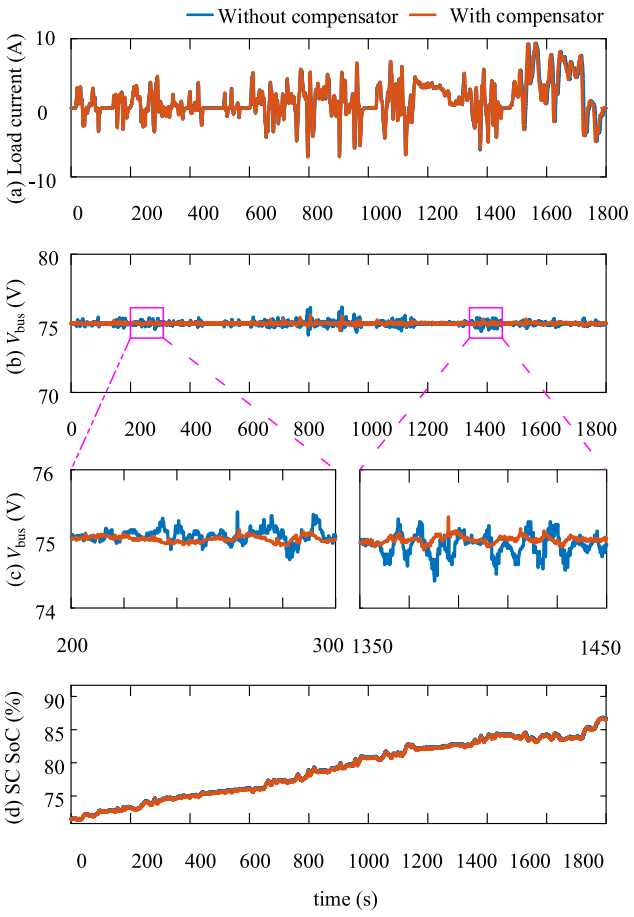


**Fig. 13.** Experimental results under constant cut-off frequency $f_c$ = 0.04 Hz. (a) Load current; (b) DC bus voltage; (c) DC bus voltage for [200, 300] s and [1350, 1450] s; (d) Supercapacitor SoC.

When the load disturbance compensator is applied, the DC bus voltage fluctuation is significantly reduced. These observations are more clearly shown in Fig. 13(c) for the time periods of [200, 300] s and [1350, 1450] s. In summary, both the short-term and the long-term scenario results show that the proposed load disturbance compensator can significantly reduce the DC bus voltage variation caused by the load current change compared to the conventional PI controller without the load disturbance compensator.

### 4.3. Validation of adaptive power split strategy

To verify the effectiveness of the adaptive power split strategy, the SC SoC under constant and adaptive cut-off frequencies are compared. The results are shown in Fig. 14. A constant cut-off frequency of 0.04 Hz is used as the baseline. Under this constant cut-off frequency, the SC SoC increases from 72% to approximately 87%, as shown in Fig. 14(d). The SC may experience over-charge if this drive cycle continues to repeat more times. When the adaptive cut-off frequency is applied, the SC SoC is controlled in the desired range. In fact, the SC SoC varies from 72% to 77% with the adaptive cut-off frequency, as shown in Fig. 14(d). In the meantime, Figs. 14 (b) and (c) show that the DC bus voltage variation is reduced by the load disturbance compensator when the adaptive cut-off frequency is applied. Therefore, with the proposed adaptive power split strategy and the load disturbance compensator, the control performance of the hybrid FC/SC power system in electric vehicles are significantly improved.

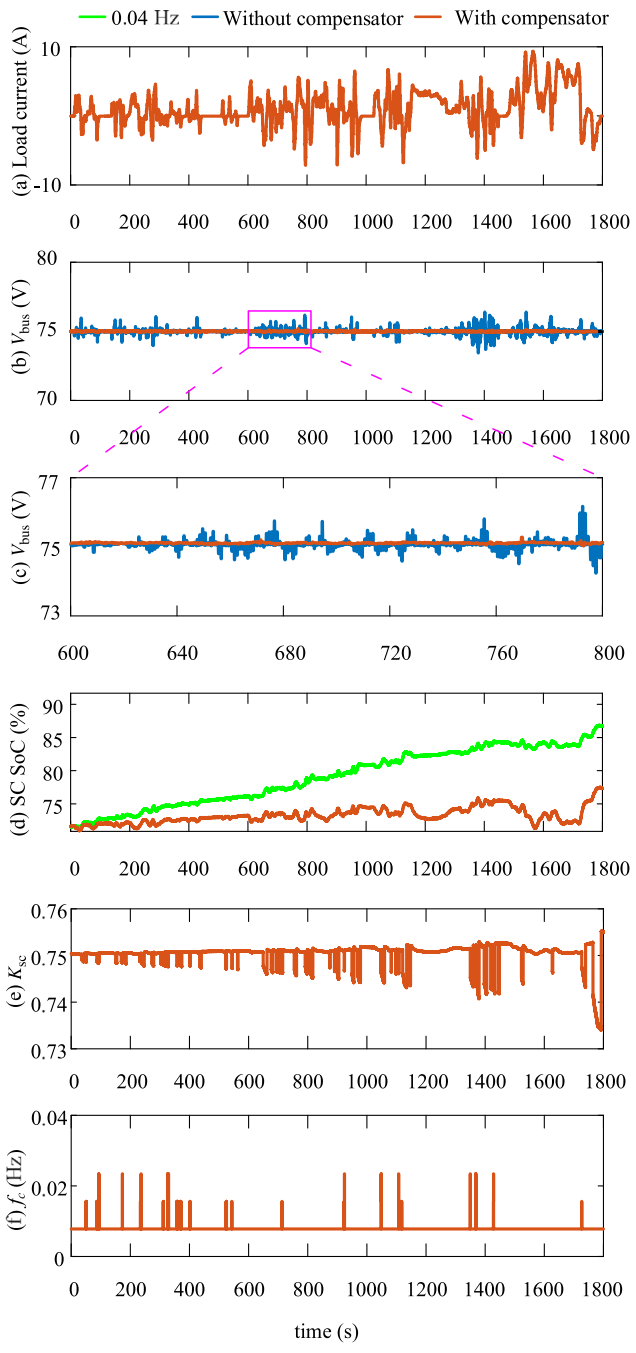


**Fig. 14.** Experimental results for adaptive power split strategy validation. (a) Load current; (b) DC bus voltage under adaptive cut-off frequency; (c) DC bus voltage under adaptive cut-off frequency for [600, 800] s; (d) Supercapacitor SoC under constant cut-off frequency of 0.04 Hz and adaptive cut-off frequency; (e) $K_{sc}$; (f) Cut-off frequency.

## 5. Conclusion

In this paper, an adaptive power split strategy with a load disturbance compensator is developed for the FC/SC hybrid power system in an electric vehicle. The adaptive power split method is proposed to smooth the FC current and prevent the SC from being over-charged and/or over-discharged. The cut-off frequency in the low-pass filter is adaptively controlled by the spectrum area ratio, which is determined by the SC SoC level. Experimental results show that the SC SoC is effectively controlled within the desired range by adaptively controlling the current distribution between the FC and the SC. The load disturbance compensator improves the control performance of the FC/SC hybrid system that the DC bus voltage fluctuation caused by the load current variation is significantly reduced. The proposed method can be easily tailored to other types of hybrid power systems.

Future work related to this topic will be focused on three aspects. First, optimized energy management needs to be introduced to achieve the minimization of hydrogen consumption and FC degradation. Second, prediction of power or energy demand should be focused to further improve the control performance. Third, an experimental comparison between the proposed scheme and the most relevant ones appearing in the literature will be performed.

## CRediT authorship contribution statement

**Qian Xun:** Investigation, conceptualization, Participated in the experiment, validation, Wrote the original draft. **Vicente Roda:** Participated in the experiment, validation. **Yujing Liu:** Investigation, conceptualization. **Xiaoliang Huang:** Conceptualization, review & editing. **Ramon Costa-Castelló:** Participated in the review & editing.

## Declaration of competing interest

The authors declare that they have no known competing financial interests or personal relationships that could have appeared to influence the work reported in this paper.

## References

[1] H.S. Das, C.W. Tan, A. Yatim, Fuel cell hybrid electric vehicles: a review on power conditioning units and topologies, Renew. Sustain. Energy Rev. 76 (2017) 268–291.
[2] J.M. Blanes, R. Gutiérrez, A. Garrigós, et al., Electric vehicle battery life extension using ultracapacitors and an FPGA controlled interleaved buck–boost converter, IEEE Trans. Power Electron. 28 (12) (2013) 5940–5948.
[3] J. Shen, A. Khaligh, A supervisory energy management control strategy in a battery/ultracapacitor hybrid energy storage system, IEEE Trans. Transp. Electrification 1 (3) (2015) 223–231.
[4] Z. Song, H. Hofmann, J. Li, et al., Optimization for a hybrid energy storage system in electric vehicles using dynamic programing approach, Appl. Energy - (139) (2015) 151–162.
[5] J. Shen, S. Dusmez, A. Khaligh, Optimization of sizing and battery cycle life in battery/ultracapacitor hybrid energy storage systems for electric vehicle applications, IEEE Trans. Ind. Inf. 10 (47) (2014) 2112–2121.
[6] Q. Xun, Y. Liu, E. Holmberg, A comparative study of fuel cell electric vehicles hybridization with battery or supercapacitor, in: Proceedings of the International Symposium on Power Electronics, Electrical Drives, Automation and Motion, SPEEDAM, 2018, pp. 389–394.
[7] H.E. Fadil, F. Giri, J.M. Guerrero, et al., Modeling and nonlinear control of a fuel cell/supercapacitor hybrid energy storage system for electric vehicles, IEEE Trans. Veh. Technol. 63 (7) (2017) 3011–3018.
[8] W. Wu, J.S. Partridge, R. Bucknall, Stabilised control strategy for PEM fuel cell and supercapacitor propulsion system for a city bus, Int. J. Hydrogen Energy 43 (2018) 12302–12313.
[9] Q. Xun, S. Lundberg, Y. Liu, Design and experimental verification of a fuel cell/supercapacitor passive configuration for a light vehicle, J. Energy Storage 33 (2021) 102110.
[10] G. Ramos, T. Montobbio de Pérez-Cabrero, Domènech-Mestres, et al., Industrial robots fuel cell based hybrid power-trains: A comparison between different configurations, Electronics 10 (12) (2021) 1431.
[11] J. Cao, A. Emadi, A new battery/UltraCapacitor hybrid energy storage system for electric, hybrid, and plug-in hybrid electric vehicles, IEEE Trans. Power Electron. 27 (1) (2012) 122–132.
[12] R. Xiong, Y. Duan, J. Cao, Q. Yu, Battery and ultracapacitor in-the-loop approach to validate a real-time power management method for an all-climate electric vehicle, Appl. Energy - (217) (2018) 153–165.
[13] B. Vural, A.R. Boynuegri, I. Nakir, et al., Fuel cell and ultra-capacitor hybridization: A prototype test bench based analysis of different energy management strategies for vehicular applications, Int. J. Hydrogen Energy 35 (2010) 11161–11171.
[14] Y. Eren, O. Erdinc, H. Gorgun, et al., A fuzzy logic based supervisory controller for an FC/UC hybrid vehicular power system, Int. J. Hydrogen Energy 34 (2009) 8681–8694.

[15] M. Uzunoglu, M.S. Alam, Modeling and anaylsis of an FC/UC hybrid vehicular power system using a novel-wavelet-based load sharing algorithm, IEEE Trans. Energy Convers. 23 (1) (2008) 263–272.
[16] P. Thounthong, S. Pierfederici, J.P. Martin, et al., Modeling and control of fuel cell/supercapacitor hybrid source based on differential flatness control, IEEE Trans. Veh. Technol. 59 (6) (2010) 2700–2710.
[17] C. Sandoval, V.M. Alvarado, J. Carmona, et al., Energy management control strategy to improve the FC/SC dynamic behavior on hybrid electric vehicles: a frequency based distribution, Renew. Energy 105 (2017) 407–418.
[18] Q. Li, B. Su, Y. Pu, et al., A state machine control based on equivalent consumption minimization for fuel cell/ supercapacitor hybrid tramway, IEEE Trans. Transp. Electrification 5 (2) (2019) 552–564.
[19] Q. Li, T. Wang, C. Dai, et al., Power management strategy based on adaptive droop control for a fuel cell-battery-supercapacitor hybrid tramway, IEEE Trans. Veh. Technol. 67 (7) (2018) 5658–5670.
[20] Q. Li, T. Wang, S. Li, et al., Online extremum seeking-based optimized energy management strategy for hybrid electric tram considering fuel cell degradation, Appl. Energy 285 (2021) 116505–116516.
[21] L. Li, C. Yang, Y. Zhang, et al., Correctional DP-based energy management strategy of plug-in hybrid electric bus for city-bus route, IEEE Trans. Veh. Technol. 64 (7) (2015) 2792–2803.
[22] M.G. Garignano, R. Costa-Castelló, V. Roda, et al., Energy management strategy for fuel cell-supercapacitor hybrid vehicles based on prediction of energy demand, J. Power Sources 360 (2017) 419–433.
[23] P. Rodaz, G. Paganelli, A. Sciarretta, et al., Optimal power management of an experiment fuel cell/supercapacitor-powered hybrid vehicle, Control Eng. Pract. 13 (2005) 41–53.
[24] Y. Yan, Q. Li, W. Chen, et al., Optimal energy management and control in mutimode equivalent energy consumption of fuel cell/supercapacitor of hybrid electric tram, IEEE Trans. Ind. Electron. 66 (8) (2019) 6065–6076.
[25] Y. Yan, Q. Li, W. Huang, et al., Operation optimization and control method based on optimal energy and hydrogen consumption for the fuel cell/supercapacitor hybrid tram, IEEE Trans. Ind. Electron. 68 (2) (2021) 1342–1352.
[26] H. He, S. Quan, F. Sun, et al., Model predictive control with lifetime constraints based energy management strategy for proton exchange membrane fuel cell hybrid power systems, IEEE Trans. Ind. Electron. 67 (10) (2020) 9012–9023.
[27] A. Soebandrio, R. Bambang, A. Rohman, et al., Energy management of fuel cell/battery/supercapacitor hybrid power sources using model predictive control, IEEE Trans. Ind. Inf. 10 (4) (2014) 1992–2002.
[28] S.N. Motapon, L.-A. Dessaint, K. Al-Haddad, A comparative study of energy management schemes for a fuel-cell hybrid emergency power system of more-electric aircraft, IEEE Trans. Ind. Electron. 61 (3) (2014) 1320–1334.
[29] F. Vivas, A. De las Heras, F. Segura, J. Andújar, A review of energy management strategies for renewable hybrid energy systems with hydrogen backup, Renew. Sustain. Energy Rev. 82 (2018) 126–155, [Online]. Available: https://www.sciencedirect.com/science/article/pii/S1364032117312418.
[30] L. Olatomiwa, S. Mekhilef, M. Ismail, M. Moghavvemi, Energy management strategies in hybrid renewable energy systems: A review, Renew. Sustain. Energy Rev. 62 (2016) 821–835, [Online]. Available: https://www.sciencedirect.com/science/article/pii/S1364032116301502.
[31] F. Zhang, X. Hu, R. Langari, D. Cao, Energy management strategies of connected HEVs and PHEVs: Recent progress and outlook, Prog. Energy Combust. Sci. 73 (2019) 235–256, [Online]. Available: https://www.sciencedirect.com/science/article/pii/S0360128519300048.
[32] X. Huang, J.M.A. Curti, Y. Hori, Energy management strategy with optimized power interface for the battery supercapacitor hybrid system of electric vehicles, in: Proceedings of IECON 2013-39th Annual Conference of the IEEE Industrial Electronics Society, 2013, pp. 4635–4640.
[33] J. Huang, Z. Huang, Y. Wu, et al., Optimal filter-based energy management for hybrid energy storage systems with energy consumption minimization, in: Proceedings of IEEE International Converence on System, Man, and Cybernetics, SMC, 2020, pp. 1822–1827.
[34] A. Florescu, S. Bacha, I. Munteanu, et al., Adaptive frequency-separation-based energy management system for electric vehicle, J. Power Sources 280 (2015) 410–4821.
[35] L. Sun, K. Feng, C. Chapman, et al., An adaptive power-split strategy for battery-supercapacitor powertrain-design, simulation, and experiment, IEEE Trans. Power Electron. 32 (12) (2017) 9364–9375.
[36] Y. Wu, Z. Huang, H. Liao, et al., Adaptive power allocation using artificial potential field with compensator for hybrid energy storage systems in electric vehicles, Appl. Energy 257 (2020) 1–14.
[37] Y. Zhou, Z. Huang, H. Liao, et al., A predictive set point modulation energy management strategy for hybrid energy storage systems, IEEE Trans. Ind. Appl. 55 (6) (2019) 6266–6277.
[38] S. Ziaeinejad, Y. Sangsefidi, A. Mehrizi-Aani, Fuel cell-based auxiliary power unit: EMS, sizing, and current estimator-based controller, IEEE Trans. Veh. Technol. 65 (5) (2016) 4286–4835.
[39] Q. Xun, Y. Liu, X. Huang, Intelligent power allocation with load disturbance compensator in fuel cell/supercapacitor system for vehicle applications, in: Proceedings of IEEE Transportation Electrification Conference & Expo, ITEC, 2020, pp. 489–494.
[40] B.P. Systems, Nexa power module user's manual MAN5100078, 2003.
[41] R.W. Erickson, D. Maksimović, Fundamentals of Power Electronics, Kluwer Academic, 2001.
[42] U. Raveendran Nair, R. Costa Castelló, A. Baños, Reset control for DC–DC converters: An experimental application, IEEE Access 7 (2019) 128487–128497, [Online]. Available: https://doi.org/10.1109/ACCESS.2019.2940140.
[43] L. Guzzella, A. Sciarretta, Vehicle Propulsion Systems. Introduction To Modeling and Optimization, Springer, Germany, 2013.
[44] K. Ramakrishnan, S. Stipetic, M. Gobbi, et al., Optimal sizing of traction motors using scalable electric machine model, IEEE Trans. Transp. Electrif. 4 (1) (2018) 314–321.
[45] Q. Xun, Y. Liu, X. Huang, et al., Drive cycle energy efficiency of fuel cell/supercapacitor passive hybrid vehicle system, IEEE Trans. Ind. Appl. 57 (1) (2021) 894–903.
[46] E. Sariyildiz, K. Ohnishi, A guide to design disturbance observer, J. Dyn. Syst. Meas. Control 136 (2) (2014) 0210111–02101110.
[47] Y. Choi, K. Yang, W.K. Chung, et al., On the robustness and performance of disturbance observes for second-order systems, IEEE Trans. Automat. Control 48 (2) (2003) 315–320.

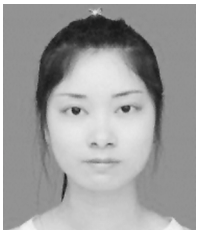

**Qian Xun** received the B.Eng. degree in automation from Hohai University, Nanjing, China, in 2012 and the M.Sc. degree in power electronics and power drives from the Nanjing University of Aeronautics and Astronautics, Nanjing, China, in 2015. She is currently working toward the Ph.D. degree with the Chalmers University of Technology, Gothenburg, Sweden. She was a Lecturer with Huzhou University, China for two years. Her research interests include modeling, simulation, control, and optimization of fuel cell hybrid electric vehicle.

**Vicente Roda** received the degree in industrial technical engineering specializing in electricity from University of Zaragoza (UZ), Spain, in 2008, the degree in hydrogen and fuel cell technologies from CIRCE Fundation, UZ, in 2008, and the degree in microsystems and intelligent instrumentation from UZ, in 2009. From 2008 to 2012, he was an In-charge of the Fuel Cell Laboratory with LIFTEC. He joined the Fuel Cell Control Group, Instituto de Robòtica e Informàtica Industrial (IRI), Barcelona, Spain in 2012.

**Yujing Liu** received the B.Sc, M.Sc., and Ph.D. degrees in electrical engineering from the Harbin Institute of Technology, Harbin, China, in 1982, 1985, and 1988, respectively. From 1996 to 2013, he was with ABB Corporate Research, Västerås, Sweden. Since 2013, he has been a Professor of Electric Power Engineering with the Chalmers University of Technology, Gothenburg, Sweden. His research intersts include motors, convertes, wireless charging for electric vehicles, generators, and power electronics for tidal power conversion.

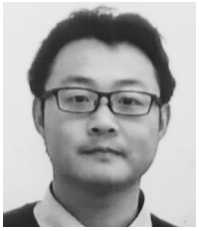

**Xiaoliang Huang** received the B.S. degree in automation engineering and the M.S. degree in control theory and control engineering from Jilin University, Changchun, China, in 2007 and 2009, respectively, and the Ph.D. degree in advanced energy from The University of Tokyo, Tokyo, Japan, in 2014. He is currently a Researcher with the Department of Electrical Engineering, Chalmers University of Technology, Gothenburg, Sweden. His current research interests include powertrain control, energy storage, and wireless power transfer for electric vehicles.

**Ramon Costa-Castelló** was born in Lleida, CATALUNYA, SPAIN in 1970. He obtained the master degree in computer science in 1993 and the PhD degree in 2001, both from UPC. Currently, he is an Associate Professor at the Automatic Control department (Department of Enginyeria de Sistemes Automàtica i Informàtica Industrial, ESAII) from UPC and the Institut de Robòtica i Informàtica Industrial, a Joint Research Center of the Spanish Council for Scientific Research (CSIC) and UPC.